

Accepted for publication in *Ap.J.* 2002 June 17

EUVE Phase-Resolved Spectroscopy of V834 Centauri

Christopher W. Mauche

*Lawrence Livermore National Laboratory,
L-43, 7000 East Avenue, Livermore, CA 94550;
mauche@cygnus.llnl.gov*

ABSTRACT

The *Extreme Ultraviolet Explorer (EUVE)* satellite was employed for 5.46 days beginning on 1999 February 9.03 UT to acquire phase-resolved EUV photometric and spectroscopic observations of the AM Her-type cataclysmic variable V834 Centauri. The resulting data are superior to those obtained by *EUVE* beginning on 1993 May 28.14 UT because the source was approximately three times brighter, the observation was four times longer and dithered, and *ASCA* observed the source simultaneously. Although we do not understand the EUV light curves in detail, they are explained qualitatively by a simple model of accretion from a ballistic stream along the field lines of a tilted ($[\beta, \psi] \approx [10^\circ, 40^\circ]$) magnetic dipole centered on the white dwarf. In 1993 when the EUV flux was lower, accretion was primarily along the $\varphi \approx \psi \approx 40^\circ$ field line, whereas in 1999 when the EUV flux was higher, accretion took place over a broad range of azimuths extending from $\varphi \approx \psi \approx 40^\circ$ to $\varphi \approx 76^\circ$. These changes in the accretion geometry could be caused by an increase in the mass-accretion rate and/or the clumpiness of the flow. The 75–140 Å *EUVE* spectra are well described by either a blackbody or a pure-H stellar atmosphere absorbed by a neutral hydrogen column density, but constraints on the size of the EUV emission region and its UV brightness favor the blackbody interpretation. The mean 1999 EUV spectrum is best fit by an absorbed blackbody with temperature $kT \approx 17.6$ eV, hydrogen column density $N_{\text{H}} \approx 7.4 \times 10^{19} \text{ cm}^{-2}$, fractional emitting area $f \approx 10^{-3}$, 70–140 Å flux $\approx 3.0 \times 10^{-11} \text{ erg cm}^{-2} \text{ s}^{-1}$, and luminosity $L_{\text{soft}} \approx 7.2 \times 10^{32} (d/100 \text{ pc})^2 \text{ erg s}^{-1}$. The ratio of the EUV to X-ray luminosities is $L_{\text{soft}}/L_{\text{hard}} \approx 40$, signaling that some mechanism other than irradiation (e.g., blob heating) dominates energy input into the accretion spot. The 1999 SW hardness ratio variation can be explained by minor variations in kT and/or N_{H} , but instead of tracking the SW count rate variation, the hardness ratio variation was sinusoidal, with a minimum (maximum) when the accretion spot was on the near (far) side of the white dwarf, consistent with the trend expected for an atmosphere with an inverted temperature distribution.

Subject headings: binaries: close — stars: individual (V834 Centauri) — stars: magnetic fields — ultraviolet: stars — white dwarfs

1. Introduction

Polars or AM Her stars are a class of semidetached binaries composed of a low-mass main-sequence secondary and a strongly magnetic ($B \approx 10\text{--}100$ MG) white dwarf primary. The strong field locks the white dwarf into corotation and the accreting matter is channeled along the field lines for much of its trajectory from the secondary's inner Lagrange point to a spot near the white dwarf magnetic pole. To match boundary conditions, the flow passes through a strong shock far enough above the star for the hot ($kT \leq kT_{\text{shock}} = 3GM_{\text{wd}}\mu m_{\text{H}}/8R_{\text{wd}} \sim 20$ keV), post-shock matter to cool and come to rest at the stellar surface. This plasma cools via bremsstrahlung and line emission in the X-ray bandpass and cyclotron emission in the optical and near-IR. Roughly half of this radiation is emitted outward and is observed directly; the other half is emitted inward, where it is either reflected or absorbed by the white dwarf surface. In addition to radiative heating, the white dwarf surface can be heated by blobs of material which penetrate to large optical depths before thermalizing their kinetic energy. For a mass-accretion rate $\dot{M} = 10^{16}$ g s⁻¹ and a relative spot size $f = 10^{-3}$, the white dwarf surface is heated to a temperature $kT = k(GM_{\text{wd}}\dot{M}/4\pi\sigma f R_{\text{wd}}^3)^{1/4} \sim 20$ eV, hence produces a radiation spectrum which peaks in the EUV.

Recent progress in our understanding of the accretion spots of polars has come from photometric and spectroscopic observations with *EUVE*. The state of our understanding of the *EUVE* spectra of polars as of mid-1998 is described by Mauche (1999), who fit blackbody, pure-H stellar atmosphere, and solar abundance stellar atmosphere models to the phase-average *EUVE* spectra of nine polars with useful data in the archive. Among the models tested, the blackbody parameterization gave the best fits to the data, with blackbody temperatures $kT_{\text{bb}} \approx 15\text{--}25$ eV and hydrogen column densities $\log N_{\text{H}}(\text{cm}^{-2}) \approx 19\text{--}20$. Wishing to increase the number of polars with good signal-to-noise ratio EUV spectra, in 1998 we obtained approval for a 130 ks *EUVE* observation of V834 Cen, whose 40 ks archival spectrum had a *peak* signal-to-noise ratio of only eight in 0.54 Å bins. Coincidentally, in late 1998 M. Ishida obtained approval for an additional *ASCA* X-ray observation of V834 Cen, so it was arranged that these observations should be obtained simultaneously. A description of the X-ray light curves and spectra from the *ASCA* observation is provided by Ishida & Fujimoto (1999) and Terada et al. (2001). Below we present the analysis of the EUV light curves and spectra from both the original 1993 and the new 1999 *EUVE* observations of V834 Cen.

V834 Cen (nee E1405–451) is a well-studied polar with an orbital period $P_{\text{orb}} = 101.5$ minutes (Mason et al. 1983) and the high ($V \approx 14$) and low luminosity states ($V \approx 17$) typical of this class of binaries. The magnetic nature of the white dwarf is demonstrated directly by the linear and circular polarization present in its high states (Cropper, Menzias, & Tapia 1986; Cropper 1989) and the Zeeman absorption features and cyclotron emission features present in its low states (Schwope & Beuermann 1990; Ferrario et al. 1992), from which a magnetic field strength of 23 MG is inferred. The distance d , white dwarf mass M_{wd} , binary inclination i , and the colatitude β and azimuth ψ of the accretion spot are all uncertain at some level, but Puchnarewicz et al. (1990) find $d > 77$ pc based on a detection of the secondary in a near-IR spectrum; Cropper et al. (1999) find $M_{\text{wd}} = 0.54\text{--}0.64 M_{\odot}$ based on fits of a *Ginga* X-ray spectrum, Ramsay (2000) finds $M_{\text{wd}} = 0.64\text{--}0.68 M_{\odot}$ based

on fits of an *RXTE* X-ray spectrum, and Schwope et al. (1993) use phase-resolved optical spectra to determine $M_{\text{wd}} = 0.66_{-0.16}^{+0.19} M_{\odot}$ for $i = 50^{\circ} \pm 10^{\circ}$; Cropper (1988) advocates $i = 45^{\circ} \pm 9^{\circ}$, $\beta = 25^{\circ} \pm 5^{\circ}$, and $\psi = 40^{\circ} \pm 5^{\circ}$ based on values compiled from the literature.

The plan of this paper is as follows. In §2 we describe the *EUVE* observations, in §3 we present the *EUVE* deep survey (DS) photometer and *ASCA* count rate light curves, in §4 we present the *EUVE* short wavelength (SW) spectrometer count rate and hardness ratio light curves, in §5 we present the mean and phase-resolved SW spectra, in §6 we provide a discussion and interpretation of these data, and in §7 we close with a summary of our results.

2. Observations

For a description of the *EUVE* satellite and instrumentation, refer to Bowyer & Malina (1991), Abbott et al. (1996), and Sirk et al. (1997). It is sufficient to note here that the bandpasses of the *EUVE* DS photometer and SW spectrometer are defined by a Lexan/Boron filter and extend from ≈ 70 to ≈ 180 Å, although, as we will see below, interstellar absorption extinguishes the EUV flux of V834 Cen longward of ≈ 140 Å. The first *EUVE* observation of V834 Cen began on 1993 May 28.14 UT, ran for 1.40 days, and resulted in a total of 42 ks of exposure, while the second observation began on 1999 February 9.03 UT, ran for 5.46 days, and resulted in a total of 161 ks of exposure. The *ASCA* observation began on 1999 February 9.96 UT, ran for 1.75 days, and resulted in a total of 58 ks of exposure. Subsequent to the first observation, a procedure was established to increase the signal-to-noise ratio of *EUVE* spectra by dithering (delightfully, to “dither” is to “shiver” or “tremble”) the pointing position of the spacecraft, thereby moving the position of the spectrum on the face of the detectors and so average over quantum efficiency variations. The first part of the second observation was erroneously performed undithered, but after 0.84 days and 25 ks of exposure the spacecraft was reconfigured to spiral dither. Unfortunately, there is no known record of the optical brightness of V834 Cen at the time of the 1993 observation, but during the 1999 observation the source was in a high optical state with $V \approx 14$ (F. M. Bateson 1999, personal communication)

As is the case for all observations of short-period CVs by low-Earth-orbit satellites, *EUVE* observations of V834 Cen are complicated by the similarity of the satellite’s orbital period ($P_{\text{sat}} \approx 94.6$ minutes) to the binary’s orbital period ($P_{\text{orb}} = 101.5$ minutes). This situation is exasperated by the fact that *EUVE* takes data only for the ≈ 30 minutes it is in Earth’s shadow. The result is that the binary phase advances by $\approx 30\%$ during each observing interval, but recedes by $\approx 7\%$ for each satellite orbit (i.e., $\phi = 0.70\text{--}1.0$, $0.63\text{--}0.93$, $0.56\text{--}0.86$, etc.). The net result is that all binary phases are sampled only after 11 satellite orbits or 0.72 days, while a full cycle is completed only after $(P_{\text{sat}}^{-1} - P_{\text{orb}}^{-1})^{-1} \approx 0.96$ days. The 1993 *EUVE* observation spans less than two such intervals, while the 1999 observation spans nearly six.

To phase these data, we assumed the spectroscopic ephemeris of Schwope et al. (1993):

$T_0(\text{HJD}) = 2445048.9500(5) + N \times 0.070497518(26)$, where N is the cycle number, T_0 is the blue-to-red zero crossing of the narrow component of the He II $\lambda 4686$ and $\text{H}\beta$ emission lines in optical spectra of V834 Cen, and the numbers in parenthesis indicate the uncertainties in the last digits; these errors result in a phase uncertainty of 0.02 (0.03) cycles at the midpoint of the 1993 (1999) *EUVE* observation. For ease of comparison, we note that Sambruna et al. (1991, 1994) used the photometric ephemeris of Cropper, Menzias, & Tapia (1986) to phase the *EXOSAT* data, and at the midpoints of the 1984, 1985, and 1986 *EXOSAT* LE + 3000 Lexan observations and the 1993 and 1999 *EUVE* observations these ephemerides differ by 0.15 ± 0.01 , 0.18 ± 0.02 , 0.19 ± 0.02 , 0.34 ± 0.05 , and 0.46 ± 0.08 cycles, respectively. The ability of the Schworer et al. ephemeris to phase the *EXOSAT* and *EUVE* light curves confirms that that ephemeris is to be preferred.

3. DS Light Curves

Assuming the above ephemeris, the 1993 and 1999 background-subtracted DS count rate light curves are as shown in the upper two panels of Figure 1. There are clear differences between the 1993 and 1999 DS light curves of V834 Cen, and although the *EUVE* light curves are similar to the 1986 and 1985 *EXOSAT* LE + 3000 Lex light curves, respectively (cf. Fig. 2 of Sambruna et al. 1994), they also differ in significant ways. Both the 1993 and 1999 *EUVE* light curves have a broad maximum peaking at binary phase $\phi \approx 0.55$, a narrow maximum peaking just before $\phi \approx 1.0$, a secondary minimum situated between the two maxima, and a strong asymmetric eclipse centered at $\phi \approx 0.88$. Compared to the 1999 light curve, the 1993 light curve has a stronger narrow maximum and a narrower, more symmetric eclipse. Conversely, the 1999 light curve has a more pronounced secondary minimum and a broader, more asymmetric eclipse.

For completeness, we show in the lower panel of Figure 1 the *ASCA* X-ray light curve obtained simultaneously with the 1999 *EUVE* observation. This light curve, kindly provided to us by M. Ishida, is the summed count rate in the 1.5–10 keV bandpass of the two *ASCA* SIS and GIS detectors. The *ASCA* light curve is seen to differ significantly from the *EUVE* light curves: it appears to consist of a double hump superposed on a constant background. The energy-resolved *ASCA* light curves of Ishida & Fujimoto (1999) and Terada et al. (2001) show that the double hump is actually a broader feature cut at low energies by an asymmetric absorption feature, which, like the *EUVE* light curves, reaches minimum at $\phi \approx 0.88$.

Because V834 Cen was a factor of approximately three times brighter in the EUV during the 1999 observation, and because its brightness was observed to dim systematically throughout the observation, we subdivided the 1999 *EUVE* observation into six equal-length intervals spanning the length of the observation, and constructed the six independent DS light curves shown in Figure 2. Modulo the overall decrease in the brightness of the source, the light curves from the various intervals generally follow the mean light curve. It is apparent from Figure 2 that during the 1999 observation the eclipse was composed of a stable, narrow (full width $\Delta\phi \approx 0.05$), full eclipse centered at $\phi \approx 0.88$, and a variable, broad, partial eclipse centered at $\phi \approx 0.79$. The largest differences

between the various intervals occur at (1) $\phi \approx 0.84$, at the interface between the partial and full eclipses, (2) $\phi \approx 0.07$, on the decline from the narrow maximum (compare the first and fifth panels of Fig. 2), and (3) $\phi \approx 0.17$, in the detailed shape of the secondary minimum: it appears at some intervals that there is a separate narrow (full width $\Delta\phi \approx 0.1$) partial eclipse situated in the valley between the two maxima.

4. SW Light Curve and Hardness Ratio

The SW spectrometer supplies an independent measurement of the EUV light curve of V834 Cen, albeit with lower signal-to-noise ratio because of the instrument’s smaller effective area and effectively higher background. Mean background-subtracted SW count rate light curves were constructed in the same manner as those of the DS with the exception that flux was collected only over the band 75–140 Å; shortward of ≈ 75 Å the background increases strongly and longward of ≈ 140 Å there is very little source flux. The resulting 1993 (1999) mean SW count rate light curve is consistent [$\chi^2/\text{degree of freedom (dof)} = 12.4/24 = 0.52$ ($\chi^2/\text{dof} = 110.4/99 = 1.12$)] with the corresponding mean DS count rate light curve after scaling the latter by a factor of 0.083 (0.079). The upper panel of Figure 3 shows the mean SW and DS count rate light curves from the 1999 observation.

To search for spectral variations associated with the variations in the count rate light curves, we constructed hardness ratio light curves by calculating the ratio of the background-subtracted SW counts from 75–95 Å to that from 95–140 Å. The break-point between the two bandpasses is arbitrary, but 95 Å was chosen because it gives roughly equal number of counts in the two bandpasses. As a compromise between phase resolution and signal-to-noise ratio, 40 phase bins were used to bin the 1999 observation, while the dimmer 1993 observation could stand no more than 10. The 1993 hardness ratio light curve can be fit by a constant 0.81 ± 0.06 with $\chi^2/\text{dof} = 6.78/9 = 0.75$, while the 1999 hardness ratio light curve, shown in the lower panel of Figure 3, is fit reasonably well by a sinusoidal function $A + B \sin 2\pi(\phi - \phi_0)$ with $A = 1.07 \pm 0.02$, $B = 0.22 \pm 0.02$, $\phi_0 = 0.19 \pm 0.02$, and $\chi^2/\text{dof} = 46.0/37 = 1.24$. The fit is significantly improved ($\Delta\chi^2 = 7.6$) even without changing the fit parameters if the isolated aberrant datum at $\phi = 0.36$ is removed from the fit. The other significant deviations from the fit coincide with the partial eclipse at $\phi \approx 0.79$ and the secondary minimum at $\phi \approx 0.17$. Surprisingly, these deviations are *downward*, in the direction of softer spectra, contrary to the behavior expected from photoelectric absorption.

5. SW Spectra

Ignoring for the moment the hardness ratio variation observed during the 1999 observation, we constructed mean SW spectra of V834 Cen from the data obtained during the two epochs of observations. The analysis procedure was similar to that described in Mauche (1999), but the

spectra were constructed from the event data and, as above, care was taken to avoid intervals when (1) the background was high, (2) the source was occulted by Earth, and (3) the SW detector was off. The spectra were binned up by a factor of 8 (from $\Delta\lambda = 0.0674 \text{ \AA}$ to 0.539 \AA) to increase the signal-to-noise ratio, to match the spectral resolution of the SW instrument (FWHM = 0.5 \AA), and to remove the nonstatistical correlation between neighboring wavelength bins. To realize the full spectroscopic potential of the 1999 observation, data from only the dithered portion of that observation (136 ks of exposure starting on 1999 February 9.88 UT) was used. The resulting mean background-subtracted SW spectra are shown in the upper panels of Figure 4, where the significantly higher quality of the 1999 spectrum is due to the three times longer exposure and three times higher mean count rate. The gross shape of these count spectra are similar, but apparent differences are masked by the effective area of the SW spectrometer, which peaks at 100 \AA and falls off at both ends of the bandpass.

To determine if the differences between these spectra are significant, we fit the data with a simple model consisting of a blackbody extinguished at long wavelengths by photoelectric absorption. For the latter, we used the EUV absorption cross sections of Rumph, Bowyer, & Vennes (1994) for H I, He I, and He II with abundance ratios of 1:0.1:0.01, as is typical of the diffuse interstellar medium. Table 1 lists the best-fit values and 90% confidence intervals of the parameters of these fits, the absorbed 70–140 \AA flux, and the fractional emitting area f and luminosity L assuming a fiducial white dwarf mass $M_{\text{wd}} = 0.7 M_{\odot}$ (hence $R_{\text{wd}} = 7.8 \times 10^8 \text{ cm}$) and a fiducial distance $d = 100 \text{ pc}$ (hence $[R_{\text{wd}}/d]^2 = 6.4 \times 10^{-24}$). The fractional emitting area is defined as the area of a circular spot on the white dwarf with open angle θ_s , divided by the full area of the white dwarf: $f \equiv 2\pi R_{\text{wd}}^2 (1 - \cos \theta_s) / 4\pi R_{\text{wd}}^2 = (1 - \cos \theta_s) / 2$; hence, the luminosity $L = 4\pi R_{\text{wd}}^2 f \sigma T^4$ and the solid angle $\Omega = \pi (R_{\text{wd}}/d)^2 \sin^2 \theta_s = 4\pi f (1 - f) (R_{\text{wd}}/d)^2$. The spectra of the best-fit models are shown superposed on the data in the upper panels of Figure 4, the residuals of the fits are shown in the lower panels of Figure 4, and the 68%, 90%, and 99% confidence contours of the fits are shown in the left panel of Figure 5. Within the context of the absorbed blackbody model, the mean spectra from these two epochs differ at the 90% confidence level, but Figure 5 shows that this is due to only a minor variation in kT and/or N_{H} .

To test the sensitivity of the fitted and inferred parameters to the assumed spectral model, we also fit the 1993 and 1999 mean SW spectra of V834 Cen with that of an absorbed, pure-H, line-blanketed, NLTE, $\log g = 8$ stellar atmosphere. A grid of 25 such models was calculated with TLUSTY v195 (Hubeny & Lanz 1995, and references therein) with temperatures distributed evenly in the log between 20 and 260 kK (1.7–22.4 eV); for the χ^2 calculations, off-grid spectra were determined by interpolation. With this model, we obtained the best-fit parameters and 90% confidence intervals listed in Table 1, and the 68%, 90%, and 99% confidence contours shown in the right panel Figure 5. As measured by χ^2/dof , these fits are just as good as the blackbody model fits, and while the range of absorbing column densities is very similar, the temperatures are much lower and the fractional emitting areas and consequently the luminosities are significantly higher. This result is a consequence of the fact that the EUV bump in the stellar atmosphere models contains

a relatively small fraction of the total luminosity, so very large spot sizes and hence very large net luminosities are required to reproduce the observed EUV fluxes. Indeed, the spot sizes are so large that they violate the geometric limit $f \leq 0.5$ over the region of parameter space shaded dark grey in Figure 5; for the pure-H stellar atmosphere model to apply, the square of the angular radius must be significantly larger than the fiducial value of $(R_{\text{wd}}/d)^2 = 6.4 \times 10^{-24}$ (i.e., V834 Cen must be significantly closer than 100 pc).

We next investigated the cause of the hardness ratio variation observed during the 1999 observation. As a compromise between phase resolution and signal-to-noise ratio, we accumulated spectra in two phase intervals centered on the minimum and maximum of the hardness ratio light curve: $\phi = 0.78\text{--}1.08$ and $\phi = 0.28\text{--}0.58$, which we imaginatively call “soft” and “hard,” respectively. The resulting background-subtracted SW spectra are shown in the upper panels of Figure 6. We fit these data with the absorbed blackbody and stellar atmosphere models discussed above and obtained the best blackbody model fits and residuals shown in Figure 6, the best-fit parameters and 90% confidence intervals listed in Table 1, and the 68%, 90%, and 99% confidence contours shown in Figure 7. As with the mean 1993 and 1999 spectra, there is significant overlap in the fit parameters of the 1999 hard and soft spectra, but the strong correlation between the model parameters results in fits which are different at significantly greater than the 99% confidence level. The largest difference between the hard and soft spectra is in the absorbing column density; indeed, for both models, the best-fit temperature of the hard spectrum is *lower* than that of the soft spectrum: within the context of these models, the hard spectrum is hard because it is more strongly absorbed. The differences between the blackbody and stellar atmosphere model fits to these data are similar to those of the 1993 and 1999 mean spectra: compared to the blackbody models, the stellar atmosphere models are far cooler, larger, and more luminous. Again, the geometric constraint $f \leq 0.5$ excludes the region of parameter space shaded dark grey in Figure 7.

Another constraint imposed on the models is the predicted value of the UV flux density. While simultaneous UV observations do not exist for either of our *EUVE* observations, V834 Cen has been observed numerous times by the *International Ultraviolet Explorer* (*IUE*) (e.g., Nousek & Pravado 1983; Maraschi et al. 1984; Takalo & Nousek 1988; Sambruna et al. 1991, 1994). We extracted all of these spectra from the *IUE* Newly Extracted Spectra (INES) data archive (<http://ines.laeff.esa.es/>) and determined that the maximum mean flux density in the nominally line-free bandpass at 1300 ± 25 Å is 4×10^{-14} erg cm $^{-2}$ s $^{-1}$ Å $^{-1}$. The intrinsic UV flux density will be larger than this value due to reddening, but unfortunately the amount of reddening is uncertain. Given the upper limit of $N_{\text{H}} = 2 \times 10^{20}$ cm $^{-2}$ for the absorbing column density from the various fits to the *EUVE* spectra, a reasonable upper limit to the reddening should be $A_V = 0.1$, but from the *IUE* spectra themselves Nousek & Pravado (1983) inferred $A_V = 0.40 \pm 0.16$; Maraschi et al. (1984) inferred $A_V < 0.47$ at the 90% confidence level; Sambruna et al. (1991) inferred $A_V = 0.10^{+0.15}_{-0.07}$; whereas Sambruna et al. (1994) inferred $A_V = 0.75$. Given this uncertainty, we consider the constraints imposed by the model UV flux densities for $A_V \leq 1, 0.3$, and 0.1 assuming the extinction curve of Fitzpatrick (1999) with $A_V/E_{B-V} = 3.1$, as is typical of the diffuse interstellar medium.

The regions of parameter space excluded by these constraints are shaded medium, light, and lighter grey, respectively, in Figures 5 and 7. Note that the UV constrains severely constrain the range of parameter space allowed to the pure-H models.

6. Discussion and Interpretation

In the previous sections we have described the phenomenology of the EUV light curves and spectra of V834 Cen measured by *EUVE* in 1993 May and 1999 February. To help understand these data, we note the following, based on our general understanding of polars and the results from optical studies of V834 Cen by Rosen, Mason, & Córdova (1987), Cropper (1988, 1989), and Schwone et al. (1993). (1) The binary inclination $i \approx 45^\circ \pm 9^\circ$ and the accretion spot colatitude and azimuth are respectively $\beta \approx 25^\circ \pm 5^\circ$ and $\psi \approx 40^\circ \pm 5^\circ$. (2) In V834 Cen only one accretion spot is visible for all orbital phases because the sum of the spot colatitude and binary inclination is less than 90° . (3) Because the binary inclination is greater than the spot colatitude, the accretion stream passes through the line of sight to the accretion region once per binary revolution. (4) The narrow and broad components of the optical emission lines of polars are understood to be due to, respectively, the heated face of the secondary and the base of the accretion stream. (5) Blue-to-red zero crossing of the narrow components of optical emission lines occurs at binary phase $\phi \approx 0$, placing the secondary (white dwarf) on the near (far) side of the binary at that phase. (6) Maximum blueshift of the broad components of optical emission lines occurs at $\phi \approx 0.42$, so at that phase the accretion stream points most directly toward us. (7) The linear polarization spike also occurs at $\phi \approx 0.42$, so at that phase the accretion column is on the plane of the sky. (8) We expect that the accretion column will point most directly toward us approximately 180° later, at $\phi \sim 0.92$. The circular polarization, EUV, and X-ray light curves are all eclipsed near this phase because of the passage through the line of sight of the (pre-shock) accretion stream and (post-shock) accretion column.

To illustrate these results, we constructed the graphic shown in the left panel of Figure 8, which includes the nominal position on the white dwarf of the accretion spot (*filled trapezoid*); the 1993 and 1999 DS light curves (*grey and black polar histograms, respectively*); and the phases of the maximum blueshift of the broad component of optical emission lines, the spike in linear polarization light curves, and the dip in circular polarization light curves. It is seen that the primary eclipse of the EUV light curves occurs when the accretion spot points toward the observer, while the dip in circular polarization light curves appears to occur *between* the primary and secondary eclipses of the EUV light curves.

To help envision the accretion geometry of V834 Cen, we constructed a simple model, shown in the right panels of Figure 8, of the path of material from the secondary's inner Lagrange point to the white dwarf surface in the vicinity of the upper magnetic pole. The model consists of the ballistic stream for a nonmagnetic semidetached binary and the field lines of a tilted magnetic dipole centered on the white dwarf for an orbital period $P_{\text{orb}} = 101.5$ minutes, mass ratio $q = 5.08$

(determining the trajectory of the ballistic stream), white dwarf mass $M_{\text{wd}} = 0.66 M_{\odot}$ (determining the white dwarf radius $R_{\text{wd}} = 8.1 \times 10^8$ cm), magnetic colatitude $\beta = 10^\circ$, and magnetic azimuth $\psi = 40^\circ$. Field lines are drawn for azimuthal angles $\varphi = 0^\circ, 10^\circ, 20^\circ, \dots, \psi + 90^\circ$. If material in the ballistic stream makes it beyond $\varphi \approx \psi + 90^\circ \approx 130^\circ$, it will accrete preferentially onto the lower magnetic pole, hence disappears from consideration. In this simple model, the material lost by the secondary travels along the ballistic stream until it is threaded by the white dwarf magnetic field; it then leaves the orbital plane and follows the magnetic field lines down to the white dwarf surface in the vicinity of the magnetic poles. In reality, the trajectory of the accreting material will be affected by the magnetic field and the magnetic field will be distorted by the accreting material; our simple model is a first-order approximation of the path of the accreting material which ignores these complications.

In the right panels of Figure 8 we see that if material accretes onto the white dwarf from the full range of possible azimuthal angles, it will produce a long, thin, arc-shaped accretion region on the white dwarf surface at the footpoints of the magnetic field lines. Details of the accretion region are more apparent in Figure 9, which shows the white dwarf and magnetic field lines for a binary inclination $i = 50^\circ$ and binary phases $\phi = 220^\circ, 230^\circ, 240^\circ, \dots, 360^\circ$ ($\phi = 0.61\text{--}1.0$). For the assumed parameters, the accretion region extends about 90° in azimuth and has a variable offset of about 20° from the magnetic pole, determined by the varying distance (a maximum of $37.5 R_{\text{wd}}$ for $\varphi = 0^\circ$ and a minimum of $5.9 R_{\text{wd}}$ for $\varphi = 130^\circ$) to the ballistic stream from the white dwarf. Accretion along the $\varphi = \psi = 40^\circ$ field line (the thick black curves in Figs. 8 and 9) will produce an accretion spot at $[\beta, \psi] = [26^\circ, 40^\circ]$, consistent with the values advocated by Cropper (1988); the other model parameters are consistent with the radial velocity solution of Schwpoе et al. (1993).

6.1. EUV Light Curves

Whether a spot or an arc, the flux at Earth from the accretion region will vary with binary phase because of the varying projected surface area of the accretion region and the phase-dependent obscuration by infalling material. Ignore for the moment obscuration and consider the simplest possible model of the EUV light curves of V834 Cen, that of a small spot “painted” on the white dwarf surface: its projected surface area hence light curve varies as $\sin i \sin \beta \cos(\phi + \psi) + \cos i \cos \beta$. Such a simple model fails to reproduce even the upper envelope of the EUV light curves of V834 Cen, and although linear a superposition of such functions (i.e., multiple spots) can reproduce some aspects of the data, the fits are not unique. Consider next an empirical model, using the EUV light curve of AM Her (Paerels et al. 1996) as a template to explain the 1999 EUV light curve of V834 Cen. Aligning the two light curves on the respective linear polarization ephemerides, the AM Her light curve reproduces well the V834 Cen light curve between binary phases $\phi \approx 0.0\text{--}0.17$. By shifting the AM Her light curve by $\Delta\phi = 0.5$, it reproduces well the V834 Cen light curve between binary phases $\phi \approx 0.17\text{--}0.6$. From this exercise, one is led to imagine that the EUV emission region of V834 Cen is composed of two spots separated in azimuth by about 180° : the first spot

produces the falling portion of the V834 Cen light curve between $\phi \approx 0.0\text{--}0.17$, while the second spot produces the rising portion of the light curve between $\phi \approx 0.17\text{--}0.6$; the remaining portion of the light curve is affected by the primary and secondary eclipses. Independent support for two accretion spots is provided by Cropper (1989), who advocates two magnetic poles separated in azimuth by about 230° to explain the occasional presence of two waves in the positional angle of the linearly polarized optical flux of V834 Cen. Such a two-spot model allows us to understand two features of the EUV light curves of V834 Cen. First, the secondary minimum at $\phi \approx 0.17$ discussed in §3 can be understood as being the interface between the falling portion of the light curve of the leading spot and the rising portion of the trailing spot. Second, the change between 1993 and 1999 in the relative strengths of the EUV light curves between phases $\phi \approx 0.0\text{--}0.17$ and $\phi \approx 0.17\text{--}0.6$ (cf. the top panel of Fig. 1) can be understood if the leading (trailing) accretion spot was brighter in 1993 (1999). Unfortunately, this model predicts that the accretion spots lie at $\phi \approx 0.05$ and $\phi \approx 0.55$, which appears not to be the case. These considerations teach us the folly of attempting to understand in detail the EUV light curves of V834 Cen (or polars in general, see Sirk & Howell 1998).

Returning to the discussion of the previous section, we expect that if the ballistic stream is threaded by the white dwarf magnetic field over a *narrow* range of azimuths, the infalling material will form a narrow stream leading down to a small spot on the white dwarf surface, whereas if the ballistic stream is threaded by the magnetic field over a *broad* range of azimuths, the infalling material will form an “accretion curtain” (as it called in intermediate polars) leading down to an extended arc on the white dwarf surface. Narrow streams are implied by the optical eclipse studies of HU Aqr and UZ For by Harrop-Allin et al. (1999) and Kube et al. (2000), respectively, but an extended accretion region is invoked by Cropper (1989) in V834 Cen to explain changes in the shape of the optical light curve and the changing morphology of the linear polarization and position angle curves. We propose that the EUV light curves of V834 Cen are explained by accretion over a narrow range of azimuths in 1993 and a broad range of azimuths in 1999. Specifically, we propose that in 1993 accretion was primarily along the $\varphi \approx \psi \approx 40^\circ$ field line, resulting in a narrow eclipse of a small accretion spot, while in 1999 accretion was more spread out in azimuth: the primary accretion channel remained the $\varphi \approx \psi \approx 40^\circ$ field line, but field lines $\approx 36^\circ$ further along the ballistic stream became active, resulting in the secondary eclipse observed at $\phi \approx 0.79$. Happily, the proposed shift of the accretion rate further along the ballistic stream qualitatively explains the reduction in the relative strength of the EUV light curve between $\phi \approx 0.0\text{--}0.17$. What caused the changes in the accretion geometry between 1993 and 1999? One option is a higher accretion rate, since in 1999 the EUV flux was approximately three times higher than in 1993. Another option is enhanced clumping of the flow, since greater clumping will result in magnetic threading over a broader range of azimuths *and* more efficient heating of the accretion spot as blobs of material crash into the stellar surface.

6.2. EUV Spectra

Although we have appealed to obscuration by the pre- and post-shock accretion flow to explain the primary and secondary eclipses in the EUV light curves of V834 Cen, Figure 3 makes clear that this obscuration cannot be due to photoelectric absorption. First, the amplitude of the SW hardness ratio variation is too small. Assuming that the mean EUV spectrum of V834 Cen is an absorbed blackbody with $kT = 17.6$ eV and $N_{\text{H}} = 7.4 \times 10^{19} \text{ cm}^{-2}$ (cf. Table 1 and Fig. 7), the SW hardness ratio equals 1.1, as observed. Doubling N_{H} decreases the SW count rate by a factor of ≈ 10 , but the SW hardness ratio increases by a factor of ≈ 4 . In contrast, during the 1999 observation, the SW count rate varied by a factor of $\gtrsim 10$ while the hardness ratio varied by only $\approx 20\%$. Similar results apply even if H and He are singly ionized, and only the He II bound-free opacity is left to absorb the EUV flux from the accretion spot. It is actually quite easy to remove the photoelectric opacity of all these ions: in a collisionally ionized plasma, H is fully ionized for $T \gtrsim 25$ kK and He is fully ionized for $T \gtrsim 100$ kK. Above that temperature, only Thomson opacity is available to reduce the EUV flux, and an electron column density $N_{\text{e}} = -\ln(0.1)/\sigma_{\text{T}} = 3.5 \times 10^{24} \text{ cm}^{-2}$ is required to reduce the EUV flux by a factor of ten. Second, the SW hardness ratio variation does not track the SW count rate variation. Instead, at least during the 1999 observation (see Fig. 3), the hardness ratio variation was sinusoidal, with a minimum (maximum) when the accretion spot was on the near (far) side of the white dwarf. Evidently, as the accretion spot rotates to the far side of the white dwarf, its spectrum systematically hardens. Figure 7 shows that the detailed spectral fits indicate that this change is best explained by decreasing kT and increasing N_{H} , but within the 68% contours this can be accomplished simply by increasing N_{H} , and within the 90% contours this can be accomplished simply by increasing kT . The last option implies that the accretion region is harder when observed at shallow viewing angles. This is the trend expected for an accretion spot subjected to irradiation by the million-degree plasma in the accretion column (van Teeseling, Heise, & Paerels 1994), although the effect is predicted to be small in the 75–140 Å bandpass and the large ratio of hard to soft X-ray luminosities (see below) argues that irradiation does not dominate the energy deposition into the accretion spot.

The mean 1993 and 1999 and the phase-resolved 1999 *EUVE* spectra of V834 Cen can be fit by a blackbody or a pure-H stellar atmosphere model absorbed by a neutral hydrogen column density with the parameters listed in Table 1. Compared to the blackbody models, the stellar atmosphere models are cooler, larger, and more luminous. In fact, as shown by Figures 5 and 7, the stellar atmosphere models are *too* big and *too* luminous (too bright in the UV) to explain the observations of V834 Cen. First, the stellar atmosphere model fails to account for the EUV spectrum acquired during the hard phase of the 1999 observation because the required angular size is larger than that of the white dwarf. Second, the stellar atmosphere model fails to account for the mean 1999 EUV spectrum because it produces too much flux in the UV unless the reddening $A_V \geq 1$. Similar problems are met applying this model to other polars (Mauche 1999), so we conclude that the pure-H stellar atmosphere model cannot in general explain the EUV of these magnetic CVs.

Finally, having *simultaneously* measured the EUV and X-ray spectra of V834 Cen in 1999, we

are in a position to determine the ratio of the luminosities of the accretion column and accretion spot. Table 1 shows that the absorbed blackbody fit to the mean 1999 EUV spectrum yields best-fit parameters $kT \approx 17.6$ eV, $N_{\text{H}} \approx 7.4 \times 10^{19}$ cm $^{-2}$, fractional emitting area $f \approx 10^{-3}$, 70–140 Å flux $\approx 3.0 \times 10^{-11}$ erg cm $^{-2}$ s $^{-1}$, and luminosity $L_{\text{soft}} \approx 7.2 \times 10^{32} (d/100 \text{ pc})^2$ erg s $^{-1}$. The averaged 2–10 keV flux measured by *ASCA* was 1.5×10^{-11} erg cm $^{-2}$ s $^{-1}$ (Ishida & Fujimoto 1999), implying $L_{\text{hard}} \approx 1.8 \times 10^{31} (d/100 \text{ pc})^2$ erg s $^{-1}$, hence $L_{\text{soft}}/L_{\text{hard}} \approx 40$ (to within a factor of ≈ 2). This imbalance between the soft accretion spot and hard accretion column luminosities is the famous “soft X-ray problem,” and signals that some mechanism other than irradiation (e.g., blob heating) dominates energy deposition into the accretion spot.

7. Summary

We have described *EUVE* observations of V834 Cen obtained in 1993 May and 1999 February. The 1999 data are superior to those obtained in 1993 because the source was approximately three times brighter, the observation was four times longer and dithered, and *ASCA* observed the source simultaneously. Although we do not understand the EUV light curves in detail, they are explained qualitatively by a simple model of accretion from a ballistic stream along the field lines of a tilted ($[\beta, \psi] \approx [10^\circ, 40^\circ]$) magnetic dipole centered on the white dwarf. In 1993 when the EUV flux was lower, accretion was primarily along the $\varphi \approx \psi \approx 40^\circ$ field line, whereas in 1999 when the EUV flux was higher, accretion took place over a broad range of azimuths extending from $\varphi \approx \psi \approx 40^\circ$ to $\varphi \approx 76^\circ$. These changes in the accretion geometry could be caused by an increase in the mass-accretion rate and/or the clumpiness of the flow. The 75–140 Å *EUVE* spectra are well described by either a blackbody or a pure-H stellar atmosphere absorbed by a neutral hydrogen column density, but constraints on the size of the EUV emission region and its UV brightness favor the blackbody interpretation. The mean 1999 EUV spectrum is best fit by an absorbed blackbody with temperature $kT \approx 17.6$ eV, hydrogen column density $N_{\text{H}} \approx 7.4 \times 10^{19}$ cm $^{-2}$, fractional emitting area $f \approx 10^{-3}$, 70–140 Å flux $\approx 3.0 \times 10^{-11}$ erg cm $^{-2}$ s $^{-1}$, and luminosity $L_{\text{soft}} \approx 7.2 \times 10^{32} (d/100 \text{ pc})^2$ erg s $^{-1}$. The ratio of the EUV to X-ray luminosities is $L_{\text{soft}}/L_{\text{hard}} \approx 40$, signaling that some mechanism other than irradiation (e.g., blob heating) dominates energy input into the accretion spot. The 1999 SW hardness ratio variation can be explained by minor variations in kT and/or N_{H} , but instead of tracking the SW count rate variation, the hardness ratio variation was sinusoidal, with a minimum (maximum) when the accretion spot was on the near (far) side of the white dwarf, consistent with the trend expected for an atmosphere with an inverted temperature distribution.

Special thanks are due to F. Bateson, Director of the VSS/RASNZ, for helping us plan the 1999 *EUVE* and *ASCA* observations of V834 Cen by instituting a program of optical observations of the source, and then regularly supplying us with visual magnitudes estimates. We thank M. Ishida for graciously supplying the *ASCA* data shown in Figure 1, S. Howell for kindly supplying the

ballistic stream trajectory shown in Figure 8, and S. Howell, K. Mukai, and P. Szkody for helpful discussions. Dispensation to schedule the *EUVE* observations during the *ASCA* observations was kindly granted by *EUVE* Project Scientist R. Malina. The *EUVE* observations were scheduled and performed by *EUVE* Science Planner M. Eckert, the staff of the *EUVE* Science Operations Center at CEA, and the Flight Operations Team at Goddard Space Flight Center. We acknowledge with thanks the use in this research of INES data from the *IUE* satellite. The manuscript was improved by the comments and suggestions of the anonymous referee. This work was performed under the auspices of the U.S. Department of Energy by University of California Lawrence Livermore National Laboratory under contract No. W-7405-Eng-48.

REFERENCES

Abbott, M. J., et al. 1996, *ApJS*, 107, 451

Bowyer, S., & Malina, R. F. 1991, in *Extreme Ultraviolet Astronomy*, ed. R. F. Malina & S. Bowyer (New York: Pergamon), 397

Cropper, M. 1988, *MNRAS*, 231, 597

Cropper, M. 1989, *MNRAS*, 236, 935

Cropper, M., Menzies, J. W., & Tapia, S. 1986, *MNRAS*, 218, 201

Cropper, M., Wu, K., Ramsay, G., & Kocabiyik, A. 1999, *MNRAS*, 306, 684

Ferrario, L., Wickramasinghe, D. T., Bailey, J., Hough, J. H., & Tuohy, I. R. 1992, *MNRAS*, 256, 252

Fitzpatrick, E. L. 1999, *PASP*, 755, 63

Harrop-Allin, M. K., Cropper, M., Hakala, P. J., Hellier, C., & Ramseyer, T. 1999, *MNRAS*, 308, 807

Hubeny, I., & Lanz, T. 1995, *ApJ*, 439, 875

Ishida, M., & Fujimoto, R. 1999, *Astron. Nachr.*, 320, 352

Kube, J., Gänsicke, B. T., & Beuermann, K. 2000, *A&A*, 356, 490

Maraschi, L., et al. 1984, *ApJ*, 285, 214

Mason, K. O., et al. 1983, *ApJ*, 264, 575

Mauche, C. W. 1999, in *Annapolis Workshop on Magnetic Cataclysmic Variables*, ed. C. Hellier & K. Mukai (San Francisco: ASP), 157

Nousek, J. A., & Pravdo, S. H. 1983, *ApJ*, 266, L39

Paerels, F., Hur, M. Y., Mauche, C. W., & Heise, J. 1996, *ApJ*, 464, 884

Puchnarewicz, E. M., Mason, K. O., Murdin, P. G., & Wichramasinghe, D. T. 1990, *MNRAS*, 244, 20P

Ramsay, G. 2000, *MNRAS*, 314, 403

Rosen, S. R., Mason, K. O., & Córdova, F. A. 1987, *MNRAS*, 224, 987

Rumph, T., Bowyer, S., & Vennes, S. 1994, *AJ*, 107, 2108

Sambruna, R. M., et al. 1991, *ApJ*, 374, 744

Sambruna, R. M., Parmar, A. N., Chiappetti, L., Maraschi, L., & Treves, A. 1994, *ApJ*, 424, 947

Schwope, A. D., Thomas, H.-C., Beuermann, K., & Reinsch, K. 1993, *A&A*, 267, 103

Schwope, A. D., & Beuermann, K. 1990, *A&A*, 238, 173

Sirk, M. M., Vallerga, J. V., Finley, D. S., Jelinsky, P., & Malina, R. F. 1997, *ApJS*, 110, 347

Sirk, M. M., & Howell, S. B. 1998, *ApJ*, 506, 824

Takalo, L. O., & Nousek, J. A. 1988, *ApJ*, 327, 328

Terada, Y., Ishida, M., Makishima, K., & Imanari, T. 2001, *MNRAS*, 328, 112

van Teeseling, A., Heise, J., & Paerels, F. 1994, *A&A*, 281, 119

Table 1. Blackbody and Pure-H Model Fit Parameters^a

Phase	kT (eV)	N_{H} (10^{19} cm $^{-2}$)	70–140 Flux (10^{-11} erg cm $^{-2}$ s $^{-1}$)	$\log f$	L (10^{33} erg s $^{-1}$)	χ^2/dof
Blackbody Model						
1993 Mean ...	$14.5^{+9.0}_{-4.7}$	$7.7^{+4.4}_{-3.5}$	$0.9^{+3.2}_{-0.5}$	$-2.8^{+2.6}_{-2.0}$	$0.59^{+54.5}_{-0.55}$	126/119
1999 Mean ...	$17.6^{+1.6}_{-1.6}$	$7.4^{+0.8}_{-0.7}$	$3.1^{+0.8}_{-0.5}$	$-3.0^{+0.4}_{-0.4}$	$0.72^{+0.65}_{-0.28}$	179/119
1999 Hard ...	$15.9^{+2.4}_{-1.9}$	$9.1^{+1.3}_{-1.1}$	$4.3^{+1.7}_{-1.1}$	$-2.3^{+0.7}_{-0.6}$	$2.6^{+5.0}_{-1.6}$	129/119
1999 Soft	$17.6^{+4.4}_{-3.3}$	$6.6^{+1.7}_{-1.5}$	$2.1^{+1.3}_{-0.7}$	$-3.3^{+1.0}_{-0.9}$	$0.39^{+1.29}_{-0.26}$	138/119
Pure-H Model						
1993 Mean ...	$2.8^{+7.0}_{-0.8}$	$8.2^{+1.0}_{-3.6}$	$0.9^{+69.0}_{-0.9}$	$+0.7^{+1.0}_{-3.7}$	$2.4^{+3.2}_{-2.3}$	127/119
1999 Mean ...	$4.5^{+1.3}_{-1.0}$	$8.1^{+0.7}_{-0.9}$	$3.1^{+22.4}_{-2.7}$	$+0.1^{+0.4}_{-0.8}$	$3.7^{+0.4}_{-1.9}$	182/119
1999 Hard ...	$3.5^{+1.5}_{-1.0}$	$9.8^{+0.9}_{-1.2}$	$4.3^{+118}_{-4.1}$	$+0.7^{+0.7}_{-0.7}$	$5.7^{+2.8}_{-0.8}$	129/119
1999 Soft	$4.6^{+3.8}_{-1.9}$	$7.3^{+1.5}_{-1.8}$	$2.1^{+337}_{-2.0}$	$-0.1^{+1.1}_{-2.1}$	$2.7^{+1.3}_{-2.5}$	139/119

^aBest-fit values and 90% confidence intervals.

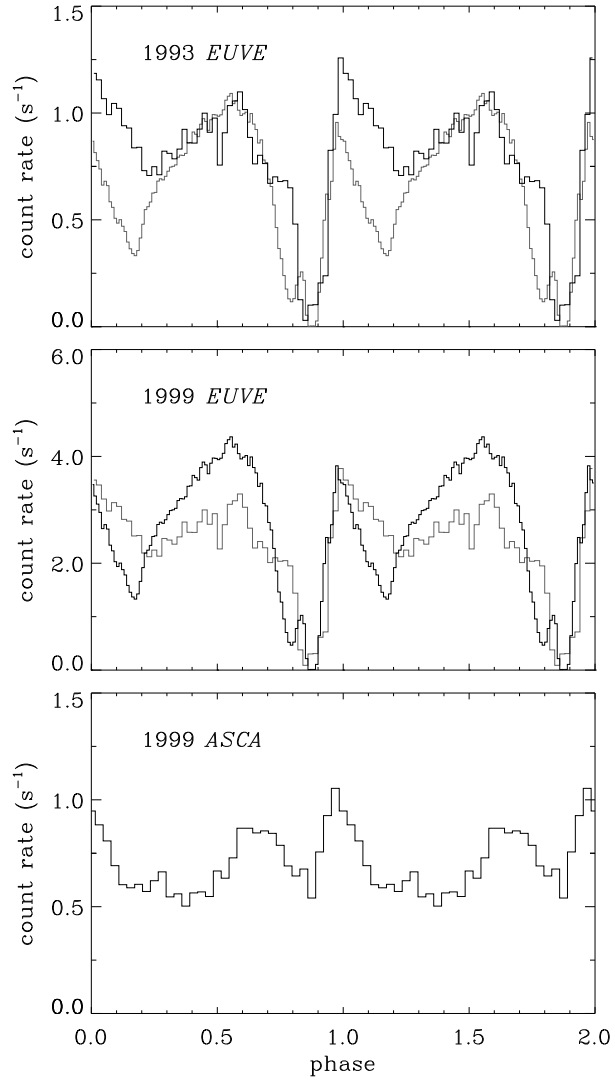


Fig. 1.— *EUVE* DS and *ASCA* SIS+GIS 1.5–10 keV count rate light curves. In the upper (middle) panel, the DS count rate light curve from the 1999 (1993) observation [scaled by 0.25 (3.0)] is shown by the grey histogram. 1σ error vectors of the 1993 and 1999 *EUVE* and *ASCA* light curves are typically 0.025–0.040, 0.030–0.055, and 0.015–0.030 counts s^{-1} , respectively.

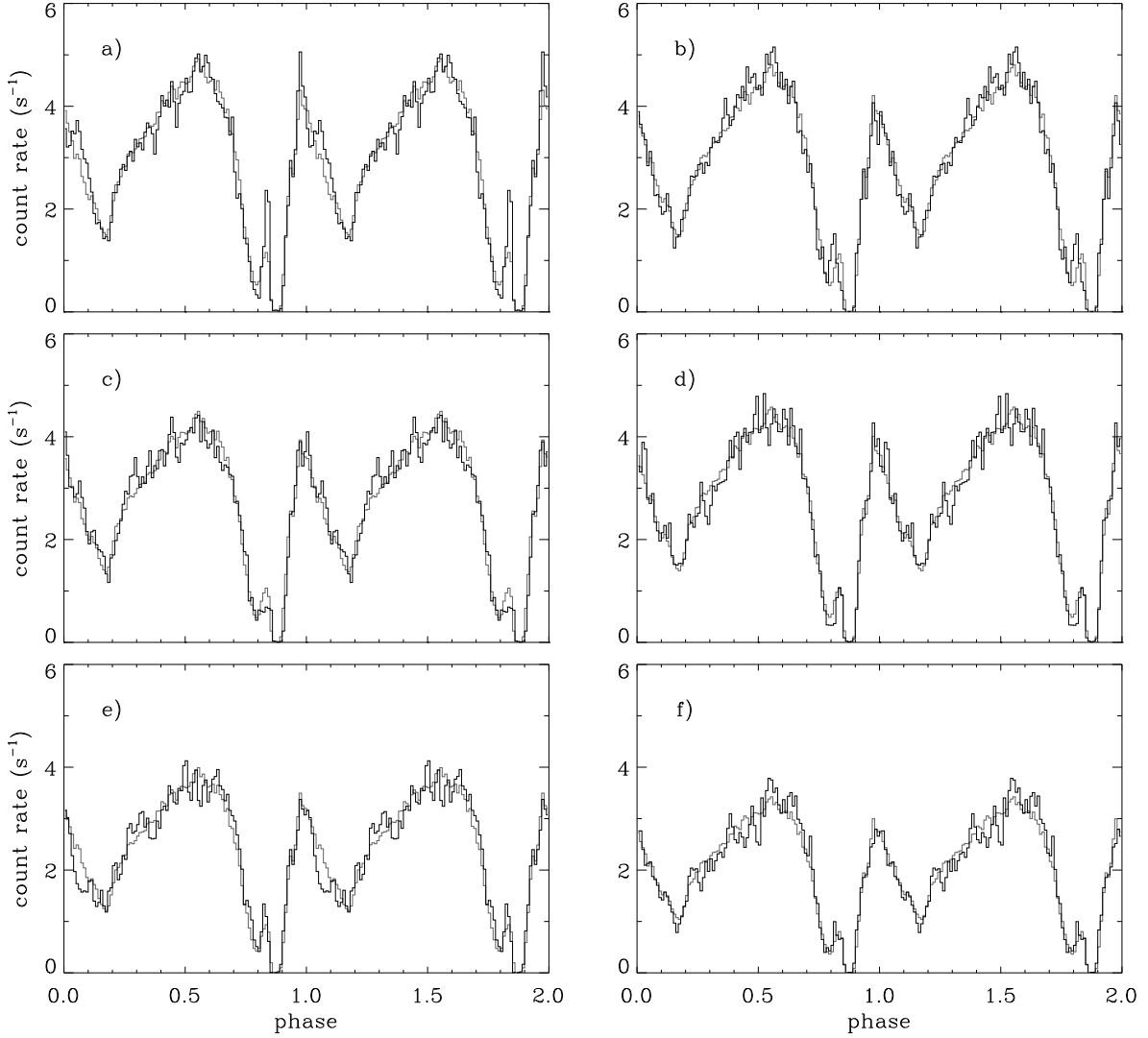


Fig. 2.— DS count rate light curves from the 1999 observation. Individual light curves are shown by the dark histograms, while the mean DS light curve (scaled by 1.13, 1.10, 1.03, 1.05, 0.91, 0.78) is shown by the grey histograms. 1σ error vectors for the individual light curves are typically $0.05\text{--}0.15$ counts s^{-1} .

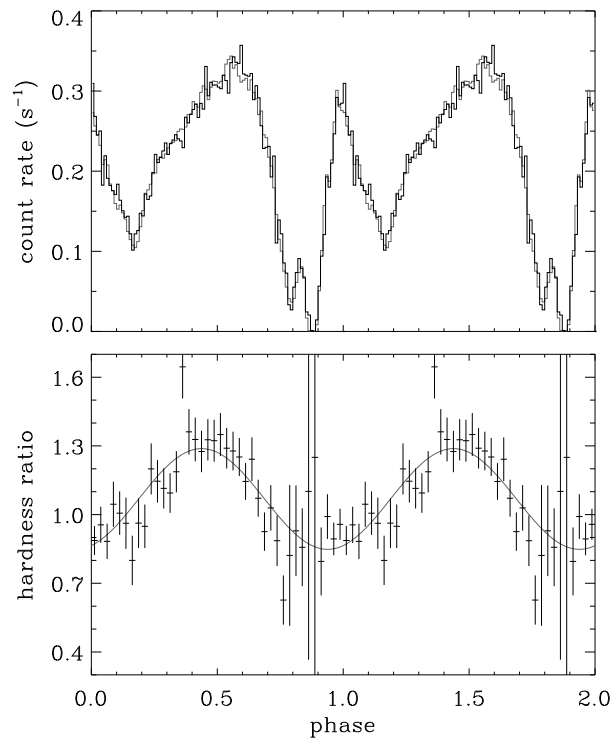


Fig. 3.— *Upper panel:* SW and DS count rate light curves from the 1999 observation. SW light curve is shown by the dark histogram, while the DS light curve (scaled by 0.079) is shown by the grey histogram. 1σ error vector of the SW light curve is typically $0.01\text{--}0.02$ counts s^{-1} . *Lower panel:* SW hardness ratio light curve H/S , where H is the count rate in the $75\text{--}95$ Å waveband and S is the count rate in the $95\text{--}140$ Å waveband. Smooth curve is the fit $H/S = 1.07 + 0.22 \sin 2\pi(\phi - 0.19)$.

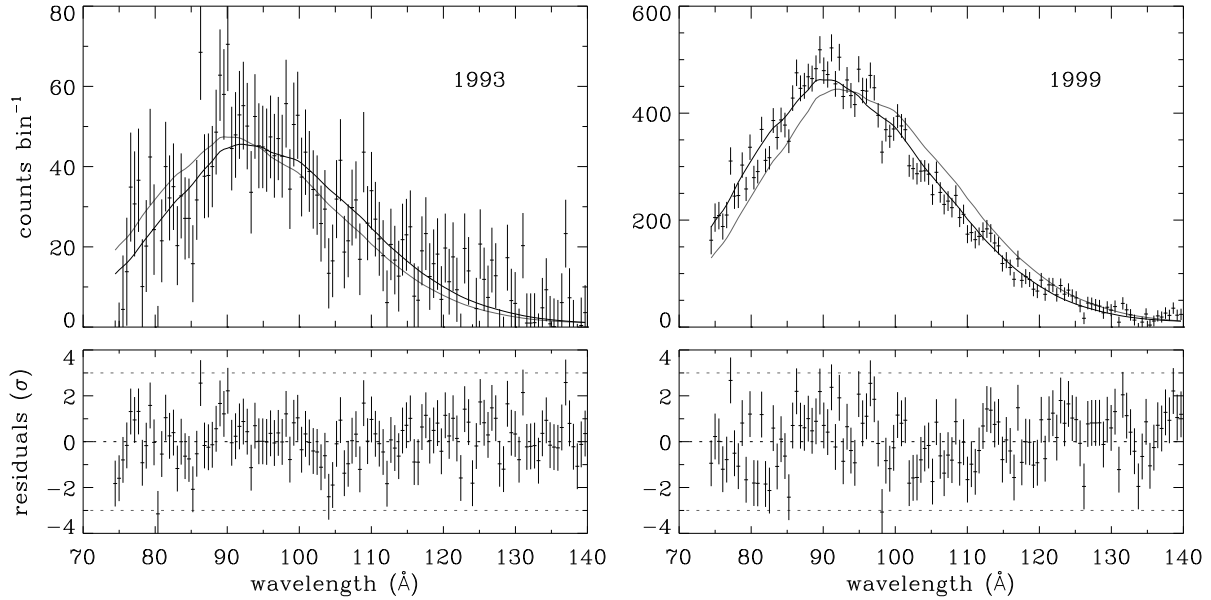


Fig. 4.— *Upper panels*: Mean SW spectra from the 1993 (*left*) and 1999 (*right*) observations. In the left (right) panel the dark curve is the best-fit blackbody spectrum of the 1993 (1999) observation, and the grey curve is the best-fit spectrum of the 1999 (1993) observation scaled by 0.10 (9.8). *Lower panels*: Residuals to the best-fit spectra.

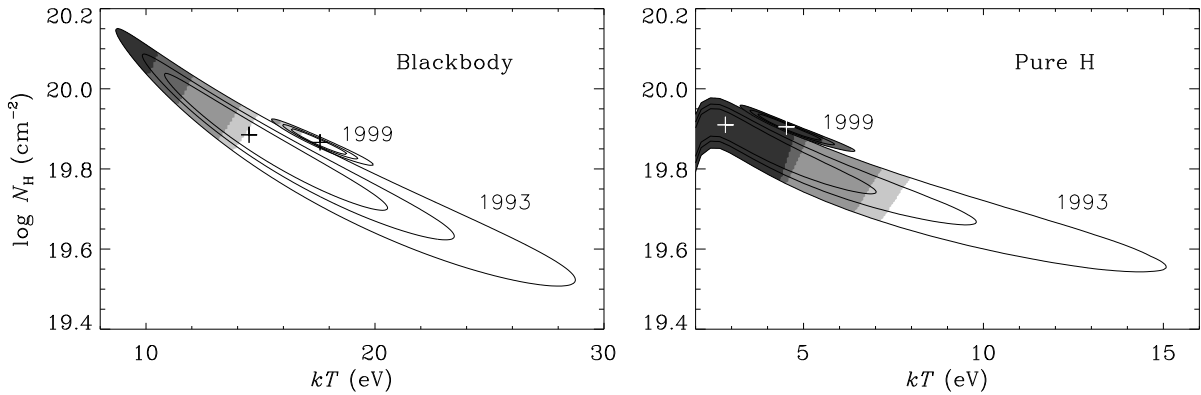


Fig. 5.— Best fit and 68%, 90%, and 99% confidence contours of the absorbed blackbody (*left panel*) and pure-H (*right panel*) model fits of the mean SW spectra from the 1993 and 1999 observations. 90% confidence intervals of the fit parameters are listed in Table 1. Regions of parameter space shaded dark, medium, light, and lighter grey are excluded by the constraints $f \leq 0.5$, $A_V \leq 1$, $A_V \leq 0.3$, and $A_V \leq 0.1$, respectively.

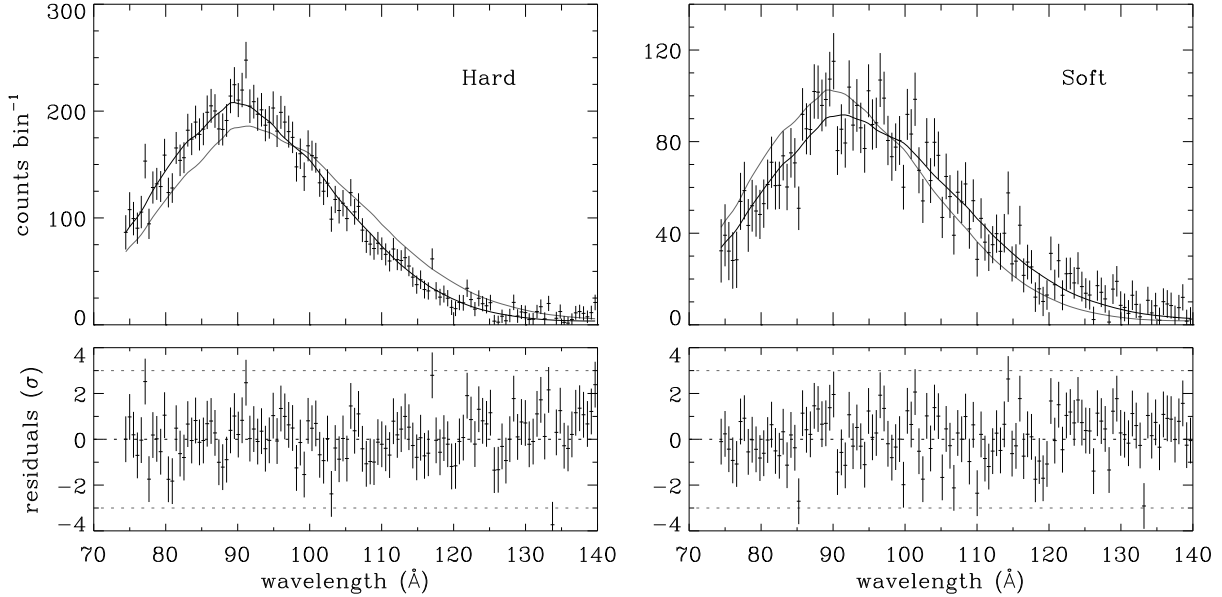


Fig. 6.— *Upper panels:* SW spectra from the hard (left) and soft (right) phases of the 1999 observation. In the left (right) panel the dark curve is the best-fit blackbody spectrum of the hard (soft) phase, and the grey curve is the best-fit spectrum of the soft (hard) phase scaled by 2.0 (0.5). *Lower panels:* Residuals to the best-fit spectra.

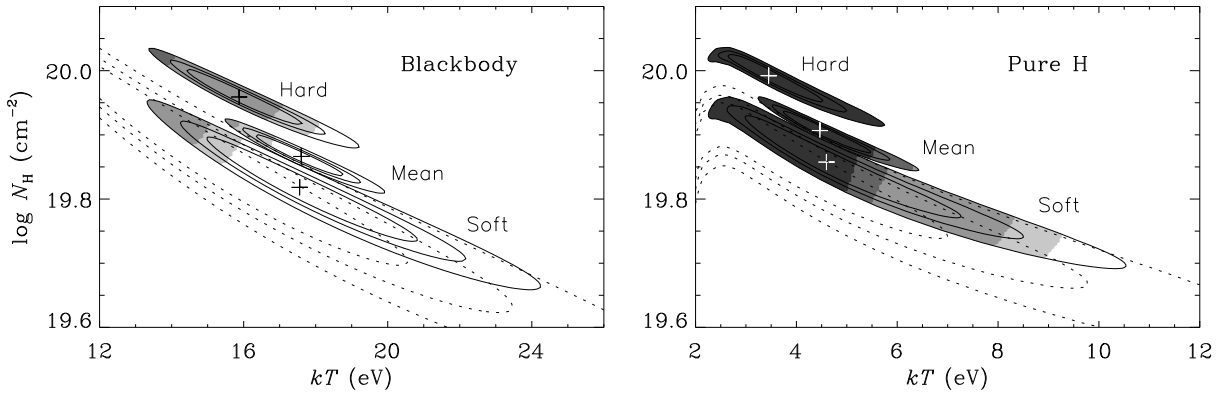


Fig. 7.— Best fit and 68%, 90%, and 99% confidence contours of the absorbed blackbody (left panel) and pure-H (right panel) model fits of the mean, hard, and soft SW spectra from the 1999 observation. Confidence contours of the mean spectrum from the 1993 observation are shown by the dotted curves. 90% confidence intervals of the fit parameters are listed in Table 1. Regions of parameter space shaded dark, medium, light, and lighter grey are excluded by the constraints $f \leq 0.5$, $A_V \leq 1$, $A_V \leq 0.3$, and $A_V \leq 0.1$, respectively.

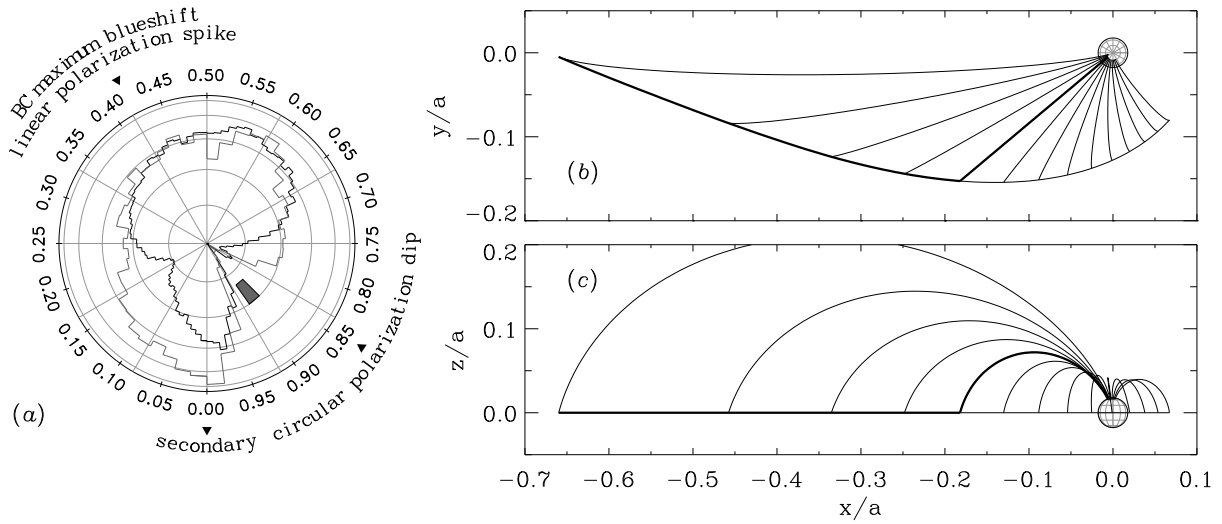


Fig. 8.— (a) Schematic diagram of the V834 Cen white dwarf showing the nominal position of the accretion spot (*filled trapezoid*); the 1993 and 1999 DS light curves (*grey and black polar histograms, respectively*); and the phases of the maximum blueshift of the broad component of optical emission lines, the spike in the linear polarization light curve, and the dip in the circular polarization light curve. Model of the white dwarf, ballistic stream, and magnetic field lines as seen from above (b) and from the side (c) for binary phase $\phi = 0.75$. Field lines for a tilted ($[\beta, \psi] = [10^\circ, 40^\circ]$) centered magnetic dipole are drawn for azimuthal angles $\varphi = 0^\circ, 10^\circ, 20^\circ, \dots, \psi + 90^\circ$. Dominant accretion path is indicated by the bold curve. Coordinates are measured relative to the semi-major axis $a = 4.6 \times 10^{10}$ cm.

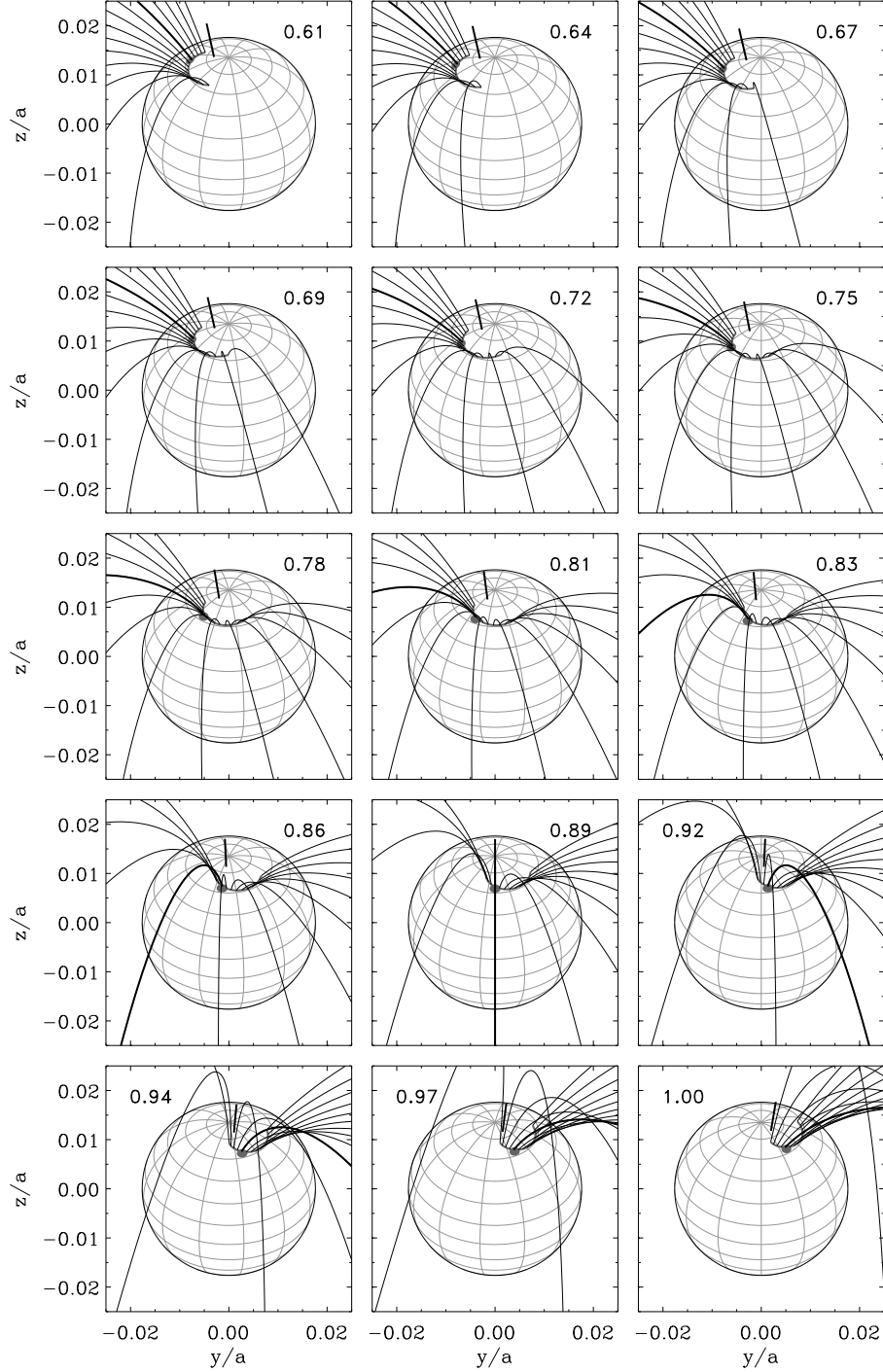


Fig. 9.— Similar to Figure 8, but showing only the white dwarf and magnetic field lines for a binary inclination $i = 50^\circ$ and binary phases $\phi = 220^\circ, 230^\circ, 240^\circ, \dots, 360^\circ$ ($\phi = 0.61-1.0$). Magnetic pole is indicated by the short thick line and a spot is suggestively drawn at the footprint of the dominant $\varphi = \psi = 40^\circ$ field line.